NUMERICAL INVESTIGATION AND DESIGN EXPLORATION ON AERODYNAMIC PERFORMANCE FOR STACKED ROTOR

Yoonpyo Hong, hyp1227@snu.ac.kr, Seoul National University (Korea)
Dawoon Lee, downl3824@snu.ac.kr, Seoul National University (Korea)
Sunwoong Yang, sleepking@snu.ac.kr, Seoul National University (Korea)
Kwanjung Yee, kjyee@snu.ac.kr, Seoul National University (Korea)

Abstract

A coaxial co-rotating (stacked) rotor can produce an improved aerodynamic efficiency compared to a coaxial counter-rotating rotor and a single-rotor with the same solidity. Since the aerodynamic performance of the stacked rotor highly depends on the relative positions of tip vortices and rotor blades, design parameters such as vertical spacing, phase angle, and pitch angle should be optimized for an operational condition. In this study, a numerical analysis through a high-order accurate Reynolds-Averaged Navier-Stokes solver was carried out to analyze the flowfields of stacked rotor configurations in a hovering condition. Design points were selected using the full factorial method with three design parameters. Exploring the wide design space revealed the full extent of performance that can be achieved through stacked rotor adjustment. The inflow and wake interference effects were turned out to be dominant factors in the aerodynamic performance of the stacked rotor system. The corresponding sectional thrust and power of each design point were modeled using a neural network. Finally, design exploration and optimization were conducted for aerodynamic efficiency.

1. INTRODUCTION

Recent developments in distributed electric propulsion and multi-rotor control technology have led to the evolution of urban air mobility (UAM) electric vertical take-off and landing (eVTOL) aircraft. The UAM eVTOL aircraft designed for city operation has various configurations that have not been attempted before (e.g., lift+cruise, wingless, vectored thrust). These configurations compensate for the shortcomings of the conventional helicopter, such as excessive aeroacoustic noise and limited flight envelope [1].

In particular, a coaxial rotor rotating in the same direction, a stacked rotor, guarantee the compactness of the aircraft and has aerodynamic advantages compared to a counter-rotating coaxial rotor or a 4-blade single rotor with the same solidity [2]. In a conventional helicopter that has coaxial rotors, the upper and lower rotors should be rotated in opposite directions for torque balance. However, because UAM eVTOL aircraft can use multiple rotors, there is no need for one coaxial rotor to have an anti-torque system. Therefore, a coaxial rotor rotating in the same direction does not need to adjust the pitch angle of the upper and lower rotors for torque balance. Also, the blade-vortex interaction that inevitably occurs when rotating in the opposite direction can be avoided [2].

Recently, studies using wind tunnel experiments and numerical analysis have been conducted to apply stacked rotors to UAM eVTOL aircraft. [3-8] Charles E. Tinney and John Valdez [3-4] conducted an experimental study comparing thrust and noise performance for the index angle. In the same case, the results of analyzing wake dynamics using particle image velocimetry were presented. Uehara et al. [5-6] conducted a comparative study on the aerodynamic performance of stacked rotors and counter-rotating coaxial rotors during hovering through experiments and RCAS. They examined the effect of induced inflow on aerodynamic performance. Rubio et al. [7] analyzed the flowfield of various types of coaxial rotors using numerical methods. Whiteside et al. [8] confirmed that the power loading of a stacked rotor could be increased than that of a single rotor under certain conditions through experiments on a small UAV-scale rotor. Also, through noise experiments, they confirmed that the stacked rotor configuration produced a reduced broadband noise. Previous studies [3-8] represent the improved aerodynamic performance of stacked rotors. Also, they show the capability of using stacked rotors in UAM eVTOL aircraft. However, their studies have some limitations: the experiments are conducted under specific test conditions [5-8], or the study cannot consider the aerodynamic efficiency due to the lack of experiment equipment. [3-4].

In this study, the aerodynamic performance of the stacked rotors is analyzed in a wide design space. Three conclusions can be achieved through this study. First, the performance achievable through stacked rotors is produced compared to the four-blade single-rotor with the same solidity. Second, the underlying physics of a stacked rotor system is analyzed using a high-order accurate Reynolds-Averaged Navier Stokes solver. Third, neural network-based design optimization is conducted to get high thrust and aerodynamic efficiency.

This research is organized in the following order: In section 2, the introduction of a numerical analysis solver and validation for a baseline rotor are presented. Design space setup and objective function definition are also produced. Section 3 analyzes the design spaces and identifies the underlying physics of a stacked rotor system. In section 4, design optimization is performed to maximize aerodynamic efficiency. Finally, section 5 presents the conclusion of the study.

2. METHODOLOGIES

2.1. Numerical approach

KFLOW[9-10], a Cartesian grid-based three-dimensional, compressible, and viscous solver, was used for numerical investigation. The high-order accurate reconstruction method, enhanced multi-dimensional limiting process for vorticity conservation(eMLP-VC)[10], was used to increase the accuracy of the vortex-dominated flow field of the stacked rotor. Through varying reconstruction methods based on the flow field characteristics, the eMLP-VC scheme can promise a high resolution of flowfield with minimal loss of accuracy. As the flux function, AUSMPW+[11] upwind scheme was used for robustness. The backward Euler method was adopted for temporal integration, assuming a steady-state. The diagonalized alternative direction inversion [12] method was used for efficient inverse matrix calculation. Also, the local time stepping method was used to accelerate the convergence. The $k-\omega$ shear stress transport model [13] was adopted as the turbulence model. It was confirmed that the result using the $\gamma-Re_\theta$ model [14] does not have a performance difference from the result using only the turbulence model.

“T-motor CF Prop 20inch” was used as the baseline rotor. The baseline rotor is commonly used in multi-rotor type aircraft. For the computational domain, 2.4 million grids per blade were used. 24 million background grids were used for the accuracy of the vortex field near the blade. The smallest grid spacing of the background grid is 0.1 mean chord length. A non-slip boundary condition was applied to the blade surface. A Riemann invariant boundary condition was applied to the far boundary. For comparison and validation of the aerodynamic performance of single rotors, the results of experiments conducted by the Korea Aerospace Research Institute and Kyungwoon University were used (not published).

The validation results are represented in Fig. 1. The Mach number of the blade tip is 0.45, and the Reynold number is 988,000. The aerodynamic performance was calculated by changing the rotation speed from 1000 revolutions per minute (rpm) to 3500rpm. The thrust and power curves for rotational speeds are shown in Fig. 1 a, b). In the case of thrust, the computational fluid dynamics (CFD) results tend to underestimate the experimental values. The required power was slightly overestimated in the power-thrust$^{1.5}$ curve (Fig. 1c). The maximum error of thrust is 5.3 percent at 3000 rpm. Fig. 1d shows the figure of merit (FM) according to blade loading. FM can be defined as follows:

$$FM = \frac{C_T^{1.5}}{\sqrt{2}C_P} \tag{1}$$

where C_T and C_P are thrust and power coefficients, respectively. The FM was calculated by changing the pitch angle. The initial pitch angle of the baseline rotor is about 2-3 degrees lower than the pitch angle of the maximum FM.

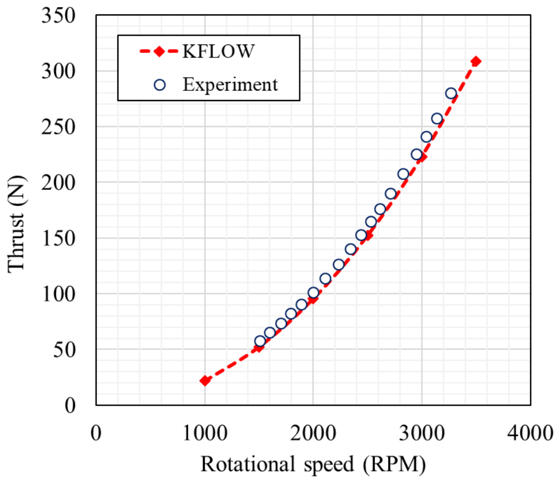

a) Thrust – rotational speed

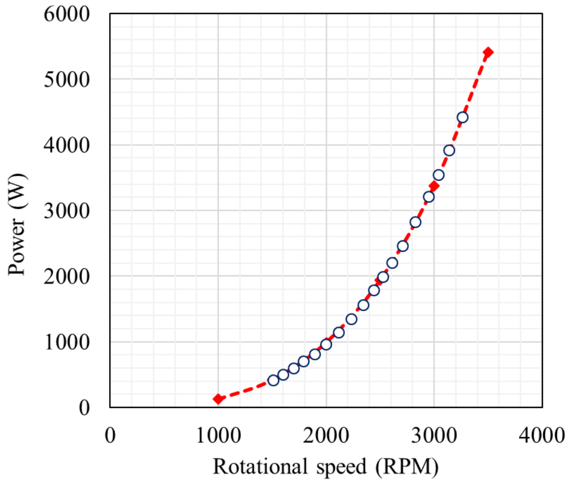

b) Power – rotational speed

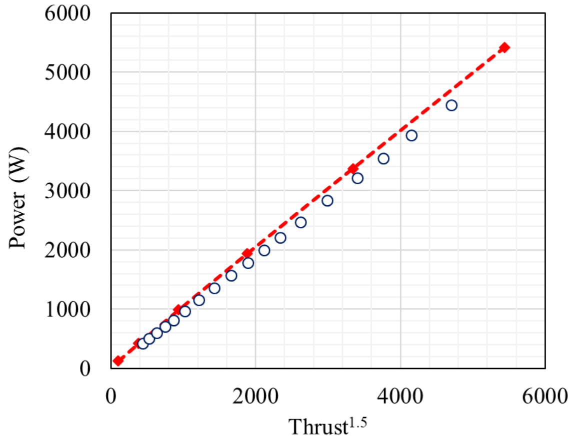

c) Power – Thrust$^{1.5}$

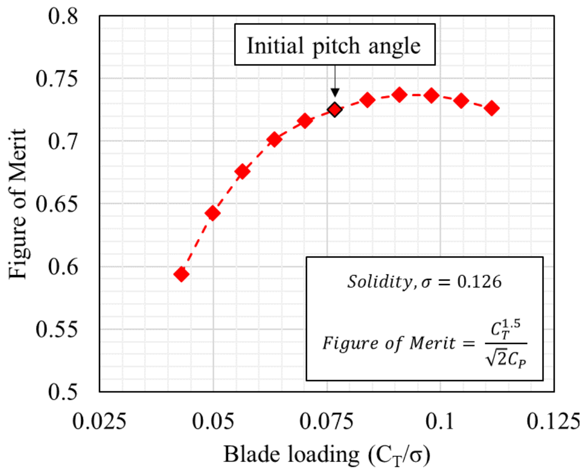

d) Figure of merit - blade loading (KFLOW)

Fig. 1 Comparison of the aerodynamic performance of baseline rotor at Tip Mach number = 0.45, Tip Reynolds number = 988,000.

2.2. Design problem setup

Three design parameters are considered as stacked rotor designs. The first parameter is the difference in pitch angle between upper and lower rotors, $\delta\theta$. If $\delta\theta$ is x°, it means that the pitch angle of an upper rotor lowers by $(x/2)$° and the pitch angle of a lower rotor raises by $(x/2)$°. The second is a vertical spacing between upper and lower rotors, δz. δz is normalized by the blade diameter, D. The last parameter is an index angle, $\delta\phi$. The positive index angle means that the lower rotor leads. The range of index angles was set as -90° to 90°. To observe the abrupt fluctuation in aerodynamic performance near 0° shown in previous studies [3-4], the interval of 5° was set near 0°. The schematic of each variable is shown in Fig. 2. The range of each variable is shown in Table 1.

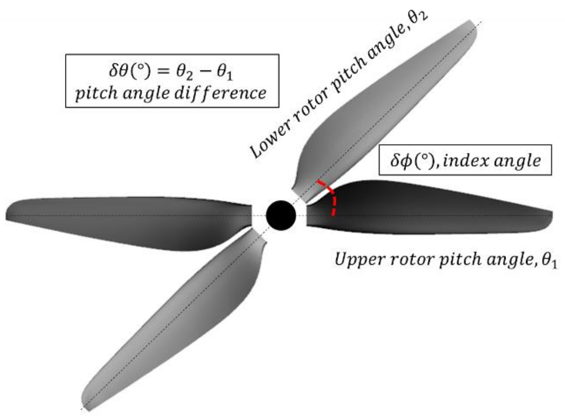

a) Top view

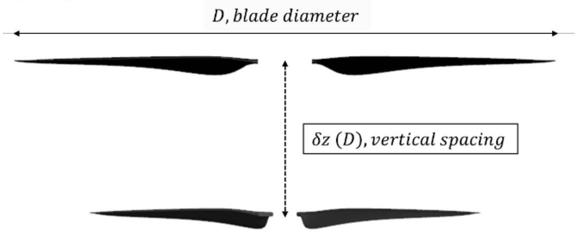

b) Side view

Fig 2. Schematic of design variables.

Table 1 Definitions and ranges of design variables

VARIABLES	DEFINITION	RANGE
$\delta\theta$ (°)	Pitch angle difference	0, 1, 2, 3, 4
δz (D)	Vertical spacing (unit = blade diameter)	0.1, 0.15, 0.2, 0.3, 0.4, 0.5
$\delta\phi$ (°)	Index angle ((+) means lower rotor leading, and (-) means upper rotor leading)	-90, -60, -45, -30, -20, -10, -5, 0, 5, 10, 20, 30, 45, 60, 90

Aerodynamic analyses were performed for 450 design of experiment (DOE) cases. The full-factorial method is used as DOE. The rotation speed is 3000 rpm for both the upper and lower rotors. The Mach number of the blade's tip is 0.45, and the corresponding Reynolds number is 988,000.

The objective function of the stacked rotor design problem is the non-dimensional power loading (C_T/C_P), a hovering performance index. The non-dimensional power loading can be defined as follows:

$$\frac{C_T}{C_P} = \frac{C_{T,total}}{C_{P,total}} = \frac{(C_{T,lower} + C_{T,upper})}{(C_{P,lower} + C_{P,upper})} \qquad (2)$$

where $C_{T,total}$ and $C_{P,total}$ is the sum of the thrust and power coefficients of the upper and lower rotors, respectively.

3. CALCULATION RESULTS DISCUSSION AND UNDERLYING PHYSICS

3.1. Numerical approach

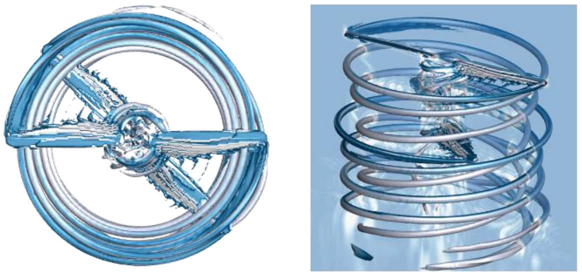

a) Iso-surface, top-view   b) Iso-surface, perspective-view

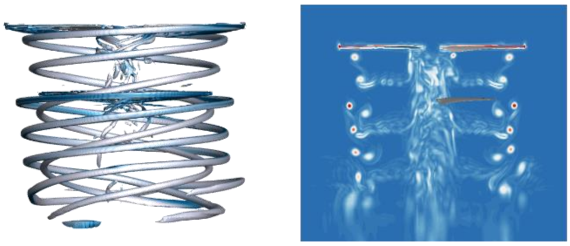

c) Iso-surface, side-view   d) Slice, vortex contour

Fig. 3 Flowfields of a stacked rotor.

All cases were calculated assuming steady-state, and converged through 14,000 iterations. The converged flowfields are the same as shown in Fig. 3. The vortices are visualized through the iso-surface method based on the Q-criterion. The tip vortices and vortex sheets of each rotor are well-resolved. Fig. 3d shows the vortex contour in the plane sliced with respect to the upper rotor. The strength and trajectory of each vortex can be figured out.

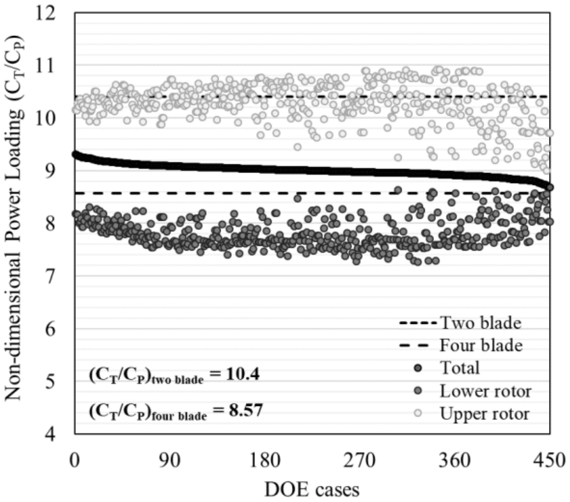

Fig. 4 Non-dimenaional power loading of DOE cases.

The results of numerical calculations are shown in Fig. 4. The non-dimensional power loadings for a total of 450 cases are represented. Maximum and minimum non-dimensional power loadings are 9.31 and 8.68, respectively. The non-dimensional power loading of the four-blade single-rotor with the same solidity is 8.57, which confirms that the performance of the four-blade single-rotor is lower than that of the stacked rotor with the lowest performance. Figure 4 also shows the performances of the isolated upper and lower blade. The isolated two-blade single-rotor has a non-dimensional power loading of 10.4. All lower rotors have lower performance than an isolated two-blade, which is mainly due to the wake effect of the upper rotor.

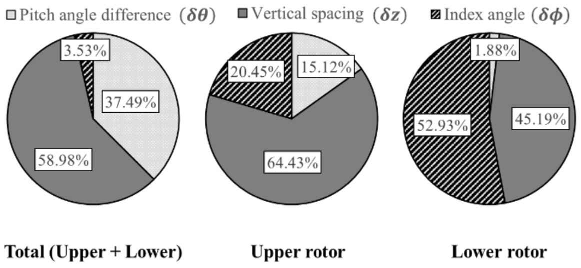

Total (Upper + Lower) **Upper rotor** **Lower rotor**

Fig. 5 ANOVA results of stacked rotors.

Fig. 5 shows the results of the analysis of variance (ANOVA) for non-dimensional power loading. The effects of $\delta\theta, \delta z,$ and $\delta\phi$ on total non-dimensional power loading are 3.53%, 59.0%, and 37.5%, respectively. ANOVA results show that the vertical spacing (δz) is the most dominant factor for the total non-dimensional power loading. On the other hand, the index angle ($\delta\phi$) has little effect on total non-dimensional power loading.

3.2. Underlying physics

Flowfield and performance analysis according to design variables were conducted for 450 cases. For detailed analysis, the effective angle of attack (α_{eff}) for each section of the blade was calculated. It was calculated in the same way as Jung et al. [15]. Two-dimensional (2D) CFD simulation was also performed to get the zero-lift angle. Sectional thrust and power distributions and vortex dynamics were analyzed. As a result, two dominant underlying physics in the stacked rotor system were discovered: 1) inflow effect and 2) wake interference effect.

3.2.1. Inflow effect

The inflow effect refers to the effect of the upper rotor on the inflow of the lower rotor and the effect of the lower rotor on the inflow of the upper rotor. In the case of the lower rotor, the upper rotor’s wake induces the downward flow to the lower rotor directly. The inflow of the lower rotor greatly increases due to the downwash of the upper rotor. As a result, the effective angle of attack of the lower blade is reduced, which can be found in Fig. 6. The effect of downwash is very strong at $r/R \leq 0.9$. On the other way, the lower rotor affects the inflow of the upper rotor. The lower rotor accelerates the wake of the upper rotor, making the wake downward speed faster. Consequently, the lower rotor makes the upper rotor inflow faster. This effect lowers the effective angle of attack of the upper rotor. Compared with the isolated single blade, the effective angle of attack distributions for both the upper and lower rotors are low in all sections, as shown in Fig. 6.

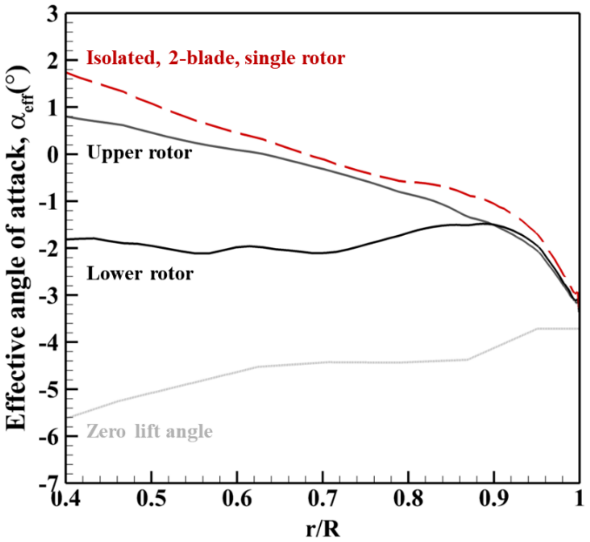

Fig. 6 Effective angle of attack distribution along the blade ($\delta z = 0.1, \delta\theta = 0°, \delta\phi = 90°$)

Figure 7 compares the flowfields of an isolated single rotor with two blades and a stacked rotor. The design variables of the stacked rotor in Fig. 7 are as follows: $\delta z = 0.1, \delta\theta = 0°, \delta\phi = 90°$. Vortex dynamics show the inflow effect directly. In the case of the stacked rotor, the miss distance is about twice that of the single rotor. The miss distances of other stacked rotor cases are also larger than that of the single rotor (not shown in this paper).

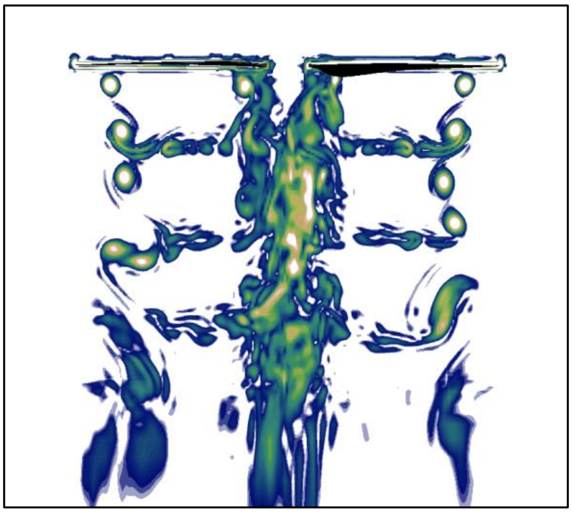

a) Isolated, two-blade, single rotor

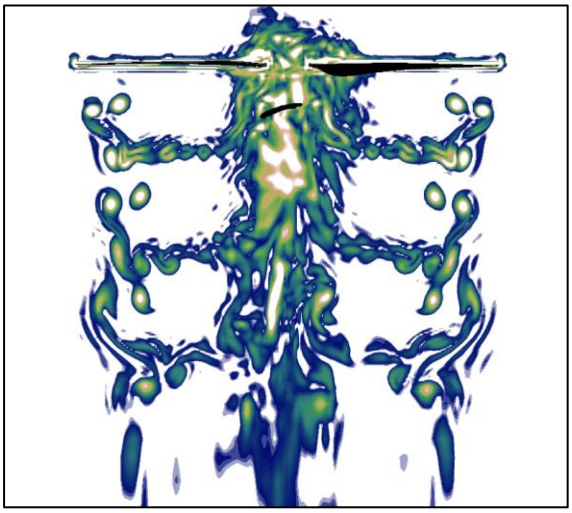

b) stacked rotor ($\delta z = 0.1D, \delta\theta = 0°, \delta\phi = 90°$)

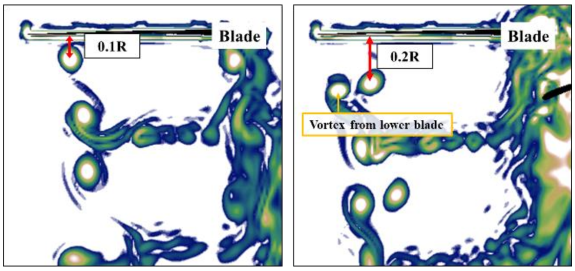

c) Comparison of the miss distance

Fig. 7 Flowfields comparison of single-rotor and stacked-rotor.

The non-dimensional power loading according to vertical spacing is shown in Fig. 8. The best performance is obtained when the vertical spacing is 0.3D.

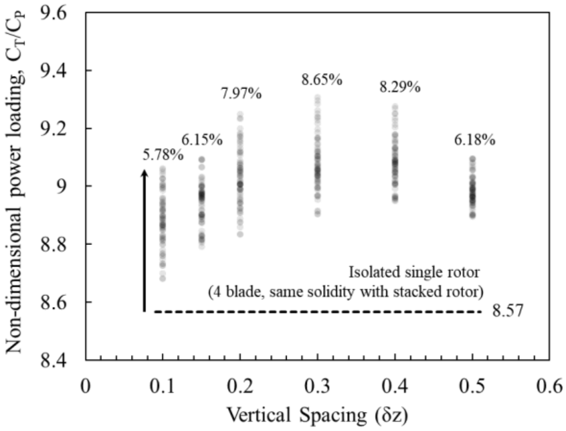

Fig. 8 Non-dimensional power loading along the vertical spacing (δz).

The sectional non-dimensional coefficients of upper and lower blades are shown in Fig. 9. As the vertical spacing increases, the aerodynamic efficiency, which is the non-dimensional power loading, increases in the upper rotor. As the vertical spacing increases, the thrust and power loading increase in all sections of the upper rotor. On the other hand, in the lower rotor, the effect changes nonlinearly. In the mid-board section, the power loading increases as the vertical spacing increases. But, in the inboard and tip section, the power loading decreases as the vertical spacing increases. The reason for these nonlinear characteristics is that the lower rotor receives not only the inflow effect but also the wake interference effect, which will be discussed next part.

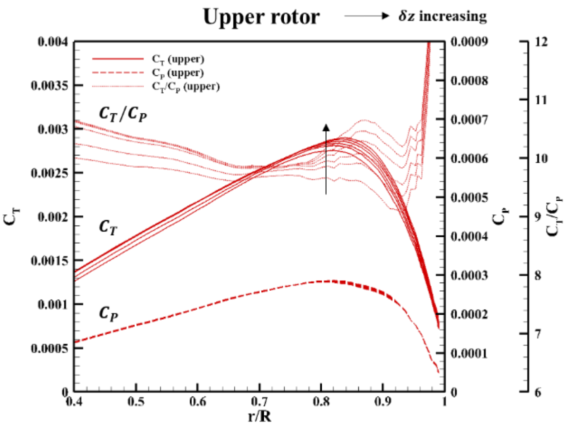

a) Upper rotor

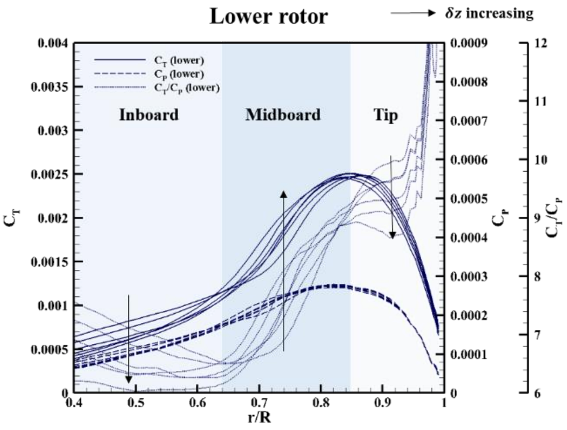

b) Lower rotor

Fig. 9 Comparison of non-dimensional coefficients along the blade

$(\delta z = 0.1{\sim}0.5, \delta\theta = 0°, \delta\phi = averaged)$

3.2.2. Wake interference effect

The wake interference effect stands for the effect on the aerodynamic performance change of the lower rotor due to the wake of the upper rotor. In Fig. 10, the peak of non-dimensional power loading appears differently depending on the phase angle. This difference is mainly due to the change in the performance of the lower rotor. When δz is $0.1D$, the peak appears when the upper rotor is leading. When δz is $0.3D$, the peak appears when the lower rotor is leading.

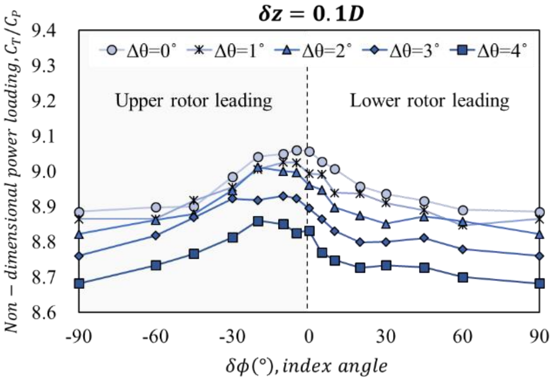

a) $\delta z = 0.1D$

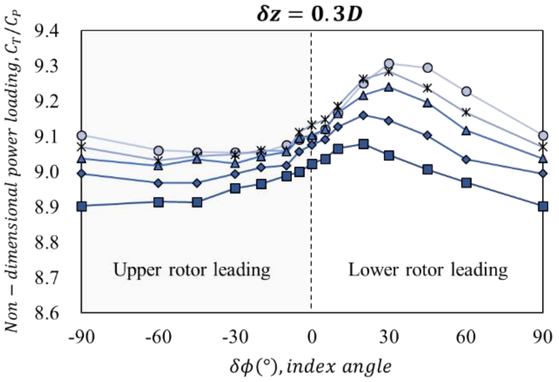

b) $\delta z = 0.3D$ (same legend in Fig. 10a)

Fig. 10 Non-dimensional power loading along the phase angle ($\delta\phi$).

Figure 11 visualizes the flowfields of the best performance cases shown in Fig. 10. Blade-vortex interactions (BVI) occur in the flowfields of both cases (Fig. 11a and 11b). The tip vortex of the upper rotor interacts with the lower rotor blade. This interaction makes a huge change in aerodynamic performances, especially the power loading. The change in aerodynamic performance according to the phase angle shown in Fig. 10 is highly related to the BVI. At the phase angle where BVI occurs, the aerodynamic performance increases. At the phase angle avoiding the BVI, the aerodynamic performance decreases. The position of the peak is changed according to δz and $\delta\theta$, which affect the tip vortex dynamics.

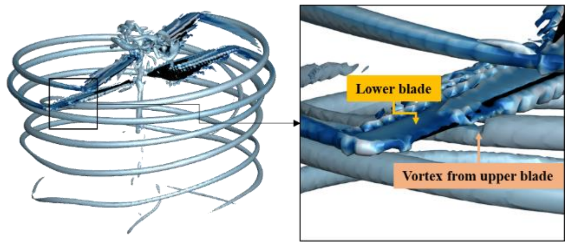

a) $\delta z = 0.1D,\ \delta\phi = -20°,\ \delta\theta = 0°$

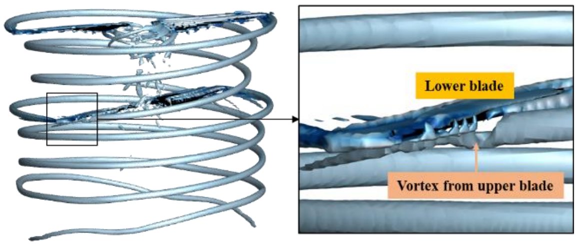

b) $\delta z = 0.3D,\ \delta\phi = 30°,\ \delta\theta = 0°$

Fig. 11 Flowfields of BVI cases (Iso-surface using Q-criterion, colored by vorticity magnitude).

Figure 12 shows the effective angle of attack distributions of stacked rotors. The cases of ($\delta\theta = 2°, \delta z = 0.3D, \delta\phi = -90{\sim}90°$) are shown. The case in red stands for the upper rotor leading cases. The blue lines stand for the cases of the lower rotor leading. The effective angle of attacks of upper rotors have little fluctuation according to $\delta\phi$. However, in the cases when the lower blade is leading, the effective angle of attack of the lower rotor changes significantly at r/R=0.7. This is the fluctuation caused by blade-vortex interaction, as seen in Fig. 11. The vortex of the upper rotor interacts with the lower rotor blade, which increases the effective angle of attack of the outboard and reduces the effective angle of attack of the inboard. Increased effective angle of attack produces high aerodynamic performance. Since the angle of attack with the highest lift-to-drag ratio in 2D airfoil is 4 to 5°, increasing the effective angle of attack induces high aerodynamic performance. Also, an increase in the effective angle of attack on the outboard side, which has faster freestream velocity, has a noticeable effect on overall aerodynamic efficiency.

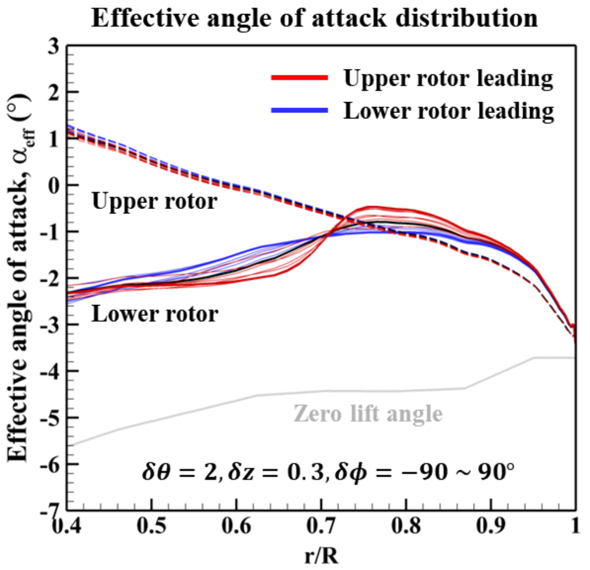

Fig. 12 Effective angle of attack distribution of stacked rotors ($\delta\theta = 2°, \delta z = 0.3D, \delta\phi = -90{\sim}90°$).

Figure 13 shows the non-dimensional coefficients for the same case as in Fig. 12. When the lower blade is leading, the sectional C_T/C_P changes significantly. The overall aerodynamic efficiency is maximized as the C_T/C_P increases on the outboard side.

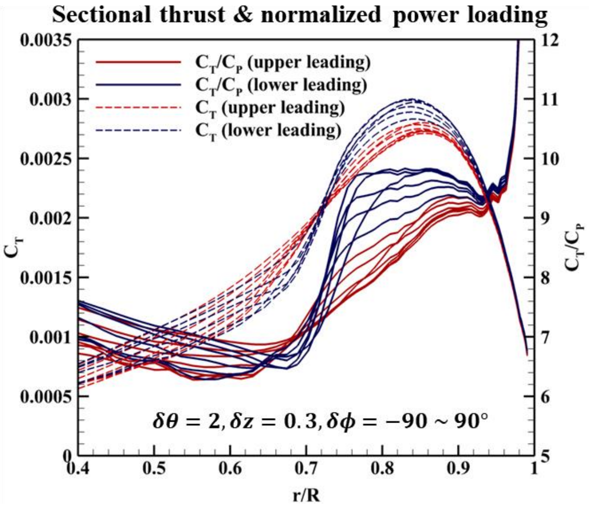

Fig. 13 Non-dimensional coefficients distribution of stacked rotors ($\delta\theta = 2°, \delta z = 0.3D, \delta\phi = -90{\sim}90°$).

4. DESIGN OPTIMIZATION

4.1. Surrogate model using neural network

A neural network was used as a surrogate model for design optimization in the current design space. For reliable design, the sectional aerodynamic coefficients of the upper and lower blades were also used for modeling. LeakyReLU was used as the activation function of the neural network model. Adam was used as the optimization technique. A total of 30,000 epochs were used. Using the learning rate scheduler, the initial learning rate was set to 0.001 and multiplied by 0.7 every 1000 epochs.

Figure 14 is a flowchart of the neural network model used in design optimization. Three design variables used in this study were set as inputs. The distributions of sectional thrust and power coefficients were modeled as a medium model. The region with r/R of 0.4 or less was excluded because the non-linearity was strong, and the freestream velocity was low so that the overall performance was not affected. As the output variables, the thrust coefficient and power coefficient of the upper and lower rotors were used. As a result of training, reliable models were created with $R^2 \geq 0.996$.

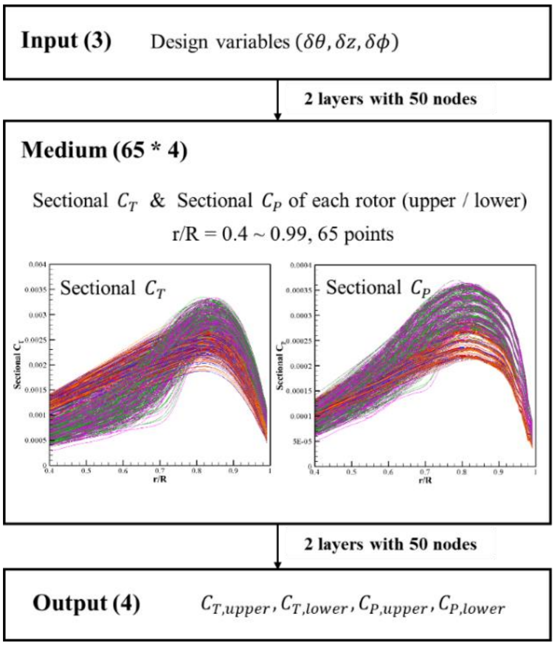

Fig. 14 A flowchart of neural network for design optimization.

4.2. Optimization results

A single objective design optimization was conducted. The objective function was set as follows:

(3) Maximize C_T/C_P

The results are summarized in Table 2.

Table 2 Results of optimization

	$\delta\theta(°)$	$\delta z(D)$	$\delta\phi(°)$	C_T/C_P
Single (4 blade)	-	-	90	8.566
Best case (DOE)	0	0.30	30	9.307
Best case (Optimized)	0	0.29	33.7	9.317

The non-dimensional power loading of the best case obtained through optimization was 9.317, which increased efficiency by 8.77% compared to a single rotor. The combination of design variables is shown in Table 2. The optimized case has a set of variables very similar to the best case of DOE. The best case of DOE shows the BVI in the lower bladem as shown in figure 11. The wake interference effect is maximized. It can be inferred that the optimized case will also be operated in a similar environment.

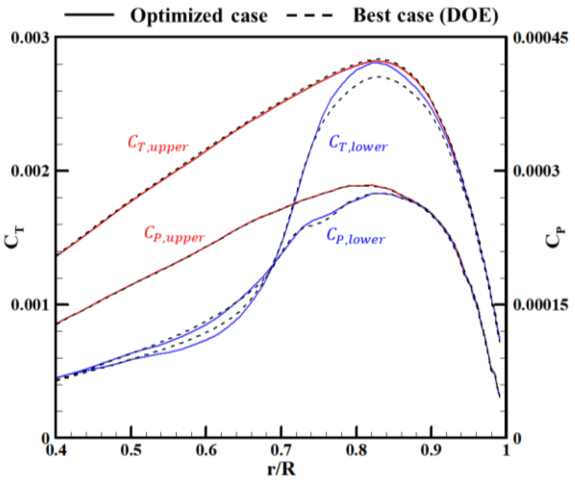

a) Sectional thrust and power coefficients

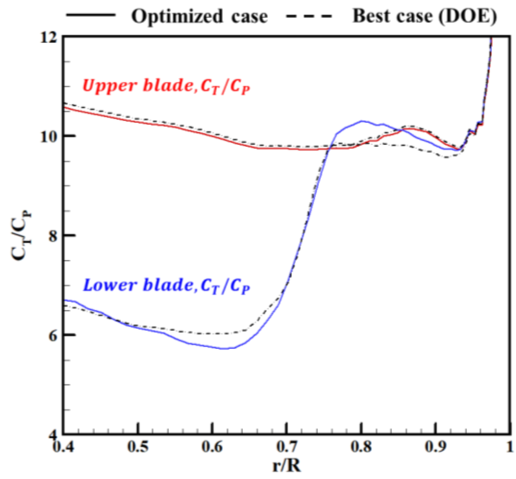

b) Sectional non-dimensional power loading

Fig. 15 Sectional aerodynamic coefficients of best cases.

Figure 15 shows the sectional coefficient distributions of the best cases. The optimized case and best case of DOE were compared. The change in the upper rotor is little, while the change in the lower rotor is significant. In the case of the optimized result, the thrust is higher on the outboard side of the lower rotor, and the thrust is lower on the inboard side. There is little change in power. An increase in thrust coefficient on the faster outboard results in higher aerodynamic efficiency. The optimized case has a stronger BVI than the base case of DOE.

The stacked rotor, unlike a counter-rotating rotor, can be operated without constraints. The operating conditions of the counter-rotating rotor are determined in consideration of anti-torque within a rotor system. However, stacked rotors do not need to consider anti-torque within a rotor system. This means that operating conditions can be changed freely, and design parameters can be adjusted for the best performance according to desired operating conditions. The Pareto front in Fig. 16 is the result of design optimization that maximizes the thrust coefficient and power. This result can be used in various ways in actual operation. For example, depending on the thrust desired, a combination of variables that will give the best aerodynamic performance can be identified. In addition, by using sectional thrust and power distribution, it is possible to find the combination that produces the best aerodynamic performance by avoiding BVI. Further research related to these applications will be carried out as a future study.

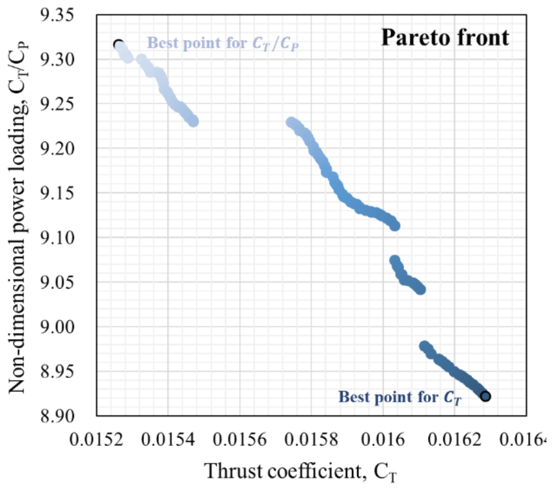

a) Pareto front of design optimization problem

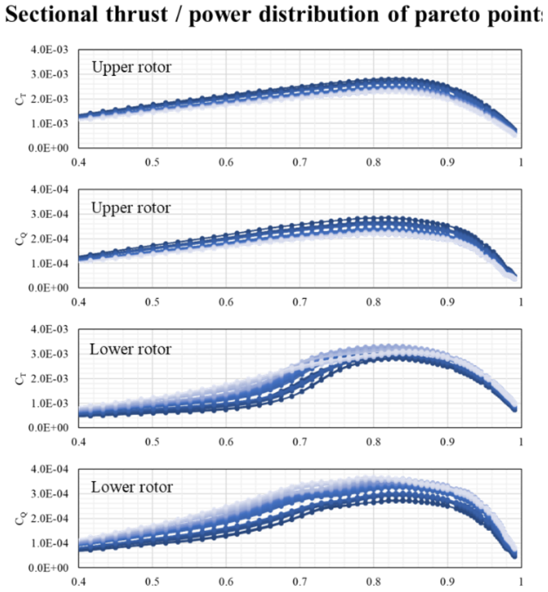

b) Sectional coefficients distribution

Fig. 16 Multi-objective design optimization results (Maximize thrust and power loading).

5. CONCLUSION

A detailed analysis of the stacked rotor configuration was conducted for aerodynamic efficiency in a hovering condition. High-order accurate CFD solver was used to investigate the whole design space of the stacked rotor. A wide range of design spaces was explored using three design variables. The inflow effect and the wake interference effect were found to be dominant underlying physics in a stacked rotor configuration. Design optimization using a neural network was performed to maximize the aerodynamic efficiency. The conclusions of this study can be summarized as follows:

1) The stacked rotor configuration can have higher aerodynamic efficiency than an isolated four-blade single rotor that has the same solidity. High fidelity calculation results of 450 cases showed an increase in efficiency of at least 1.35% and up to 8.65%.
2) Two underlying physics were identified: inflow effect and wake interference effect. The inflow effect stands for the change of inflow due to the existence of the upper and lower rotors. The upper and lower rotors influence each other's inflow, which makes both rotors' inflow stronger. The stronger inflow produces a reduced effective angle of attack and consequently deteriorates the aerodynamic efficiency. Secondly, the wake interference effect represents the upper rotor wake effect on the lower rotor. In particular, when the tip vortex of the upper rotor interacts with the lower rotor, the wake interference effect is maximized. The BVI of the lower rotor produces the increased effective angle of attack in the outboard section, which ensures the high aerodynamic efficiency of the lower rotor.
3) A neural network-based design optimization using sectional aerodynamic coefficients was performed to maximizing aerodynamic efficiency. The results show that the design variable moves in the direction where the wake interference effect becomes dominant. The optimized case has similar design variable combinations as the best case of DOE. The predicted sectional coefficients show that the optimized case has a stronger BVI than the best case of DOE and maximizes the wake interference effect.

6. ACKNOWLEDGMENTS

The authors thank Professor Soo Hyung Park for providing the KFLOW source code for the current study. This work was supported by the Ministry of Trade, Industry and Energy and Korea Institute of Energy Technology Evaluation and Planning (No. 2019281010007A, No. 20203020040010).

7. REFERENCES

[1] Rizzi, S. A., Huff, D. L., Boyd, D., Bent, P., Henderson, B., Pascioni, K. A., Sargent, C., Josephson, D. L., Marsen, M., He, H., and Snider, R., "Urban Air Mobility Noise: Current Practice, Gaps, and Recommendations," NASA TP-2020-5007433, 2019.

[2] Antcliff, K. R., Whiteside, S. K. S., Kohlman, L. W., and Silva, C., "Baseline Assumptions and Future Research Areas for Urban Air Mobility Vehicles," AIAA SciTech 2019 Forum, AIAA Paper 2019-0528, Jan. 2019.

[3] Tinney, Charles E., and John Valdez., "Thrust and Acoustic Performance of Small-Scale, Coaxial, Corotating Rotors in Hover," AIAA Journal, Vol. 58, No. 4, 2020, pp. 1657-1667.

[4] Valdez, John A., and Charles E. Tinney. "Wake of a Coaxial Corotating Rotor in Hover," AIAA Journal, 2022 (Online published).

[5] Uehara, D., and Sirohi, J., "Quantification of Swirl Recovery in a Coaxial Rotor System," American Helicopter Society 73rd Annual Forum, Vertical Flight Soc., Fairfax, VA, 2017, pp. 2828–2840.

[6] Uehara, D., Sirohi, J., and Bhagwat, M., "Hover Performance of Corotating and Counterrotating Coaxial Rotors," Journal of the American Helicopter Society, Vol. 65, No. 1, 2020, pp. 1–8.

[7] Rubio, R. C., P. V. Diaz, and S. Yoon. "High-fidelity computational analysis of ducted and coaxial rotors for urban air mobility," Proceedings of the 75th Annual Forum, Philadelphia. 2019.

[8] Whiteside, S. K. S., Zawodny, N. S., Fei, X., Pettingill, N. A., Patterson, M. D., and Rothhaar, M., "An Exploration of the Performance and Acoustic Characteristics of UAV-Scale Stacked Rotor Configurations," AIAA Scitech Forum, AIAA Paper 2019-1071, 2019.

[9] Park, S. H., and Kwon, J. H., "Implementation of K-ω Turbulence Models in an Implicit Multigrid Method," AIAA Journal, Vol. 42, No. 7, 2004, pp. 1348–1357.

[10] Hong, Y., Lee, D., Yee, K., and Park, S. H.,

"Enhanced High-Order Scheme for High-Resolution Rotorcraft Flowfield Analysis," AIAA Journal, Vol. 60, No. 1, 2022, pp. 144-159.
[11] Kim, K. H., Kim, C., and Rho, O. H., "Methods for the Accurate Computations of Hypersonic Flows: I. AUSMPW+ Scheme," Journal of Computational Physics, Vol. 174, Nov. 2001, pp. 38–80.
[12] Caughey, D. A., "Diagonal Implicit Multigrid Algorithm for the Euler Equations," AIAA Journal, Vol. 26, No. 7, 1988, pp. 841–851.

[13] Menter, F. R., "Two-Equation Eddy Viscosity Turbulence Models for Engineering Applications," AIAA Journal, Vol. 32, No. 8, 1994, pp. 1598–1605.

[14] Menter, F. R., Langtry, R. B., Likki, S. R., Suzen, Y. B., Huang, P. G., and Völker, S., „A correlation-based transition model using local variables—part I: model formulation,″ Journal of Turbomachinery, Vol. 128, No. 3, 2006, pp. 413–422.

[15] Y.S. Jung, J. Baeder, C. He,, "Investigation of Empirical Rotor Broadband Prediction using CFD Boundary Layer Parameters Extraction," Proceeding of the 77th VFS Annual Forum, Virtual Event, 2021.